

Opaque Lowermost Mantle

Sergey S. Lobanov^{1,2,*}, François Soubiran³, Nicholas Holtgrewe¹, James Badro⁴, Jung-Fu Lin⁵,
Alexander F. Goncharov¹

¹GFZ German Research Center for Geosciences, Section 3.6, Telegrafenberg, 14473 Potsdam, Germany

²Geophysical Laboratory, Carnegie Institution of Washington, Washington, DC 20015, USA

³École Normale Supérieure de Lyon, Université Lyon 1, Laboratoire de Géologie de Lyon, CNRS UMR5276, 69364 Lyon Cedex 07, France

⁴Université de Paris, Institut de Physique du Globe de Paris, CNRS, 75005 Paris, France

⁵Department of Geological Sciences, Jackson School of Geosciences, The University of Texas at Austin, Austin, Texas 78712, USA

*E-mail: slobanov@gfz-potsdam.de

ABSTRACT

Earth's lowermost mantle displays complex geological structures that likely result from heterogeneous thermal and electromagnetic interaction with the core¹⁻⁴. Geophysical models of the core-mantle boundary (CMB) region rely on the thermal and electrical conductivities of appropriate geomaterials which, however, have never been probed at representative pressure and temperature (P - T) conditions. Here we report on the opacity of single crystalline bridgmanite and ferropericlasite, which is linked to both their radiative and electrical conductivity, measured in dynamically- and statically-heated diamond anvil cells as well as computed from first-principles at CMB conditions. Our results show that light absorption in the visible spectral range is enhanced upon heating in both minerals but the rate of change in opacity with temperature is a factor of six higher in ferropericlasite. As a result, bridgmanite in the lowermost mantle is moderately transparent while ferropericlasite is highly opaque. Our measurements suggest a very low (< 1 W/m/K) and largely temperature-independent radiative conductivity in the lowermost mantle, at odds with previous studies^{5,6}. This implies that the radiative mechanism has not contributed significantly to cooling the Earth's core throughout the geologic time and points to a present-day CMB heat flow of 9-11 TW. Opaque ferropericlasite is electrically conducting and mediates strong core-mantle electromagnetic coupling, explaining the intradecadal oscillations in the length of day, low secular geomagnetic variations in Central Pacific, and the preferred paths of geomagnetic pole reversals.

MAIN TEXT

Heat flow across the CMB (Q_{CMB}) sustains all major geodynamic processes in the Earth's mantle and core. The observed vigor of modern plate tectonics, plume activity, and the geodynamo requires that the current Q_{CMB} is 8-16 TW (Ref.^{3,7}). The intensity of these geodynamic processes in the past, however, is uncertain but can be clarified if the CMB heat flow (Q_{CMB}) is reconstructed as a function of geologic time. An independent estimate of Q_{CMB} can be obtained by using the Fourier law of heat conduction: $Q_{CMB} = A_{CMB} * k_{total} * \Delta T$ (Eq. 1), where A_{CMB} is the surface area of the CMB, ΔT is the temperature gradient in the thermal boundary layer (TBL), and k_{total} is the thermal conductivity of the TBL. One key unknown is the ability of the lowermost mantle to conduct heat via light radiation, which is determined by the opacity of mantle minerals at CMB P - T conditions.

The liquid outer core and the solid mantle also interact via the exchange of angular momentum, which may cause detectable variations in the Earth's rotation. Electromagnetic coupling between the core and mantle may be responsible for the reversible change in the length of day with a period of ~ 6 years⁸ as observed by geodetic techniques. Strong coupling, however, demands that the electrical (DC) conductivity of the lower mantle minerals is sufficiently high at the CMB⁹. Furthermore, the absence of a significant lag between the rotational and magnetic signals impose a stringent limitation on the thickness of the conducting layer to be smaller than 50 kilometers⁸. Tomographic images of the lowermost mantle revealed anomalous 5-40 km thick patches directly above the core with strong seismic wave speed reductions of ($\sim 10\%$), called ultra-low velocity zones (ULVZs)⁴. Because of their location just above the CMB and small thickness, these patches may be responsible for the efficient core-mantle electromagnetic coupling, yet the electrical properties of ULVZs are unknown. The DC electrical conductivity can be constrained in optical absorption experiments by extrapolating the energy-dependent optical conductivity to zero frequency. Therefore, the radiative and DC electrical conductivity can be in principle determined in a single experiment.

Insofar, the absorption coefficients of lower mantle minerals have never been measured at CMB P - T conditions. The brightness of conventional light sources is insufficient to probe hot samples with spectral radiance corresponding to several thousand degrees Kelvin and spectroscopic measurements at the conditions of combined high P and T remain a great challenge. As a consequence, information on the spectroscopic properties of mantle minerals at high P is largely limited to $T < \sim 1000$ K. Here, we overcome the experimental limitations by employing statically- and dynamically-heated DACs coupled with laser-bright broadband pulsed optical probes and fast detectors. We report on the light absorption in single crystalline bridgmanite (Bgm), ferropericlase (Fp), and an aggregate of these minerals with realistic chemical compositions at P - T conditions representative of the lowermost mantle. We show that temperature is a major factor that governs the opacity near the base of the mantle where Bgm remains moderately transparent in the visible range while Fp is highly opaque. We reinforce our experimental findings with first-principles calculations of Fp optical properties at near CMB conditions, which constrain its absorption coefficient in the near-IR range as well as the electrical conductivity. Our results indicate extremely low radiative thermal contribution to the Q_{CMB} and have profound implications to energy transport and electromagnetic coupling across the core-mantle boundary.

First, we collected high-pressure wide spectral range absorption coefficients of double-polished single crystalline Bgm6 (Bgm with 6 mol.% Fe) and Fp13 (Fp with 13 mol.% Fe) (Extended Data Fig. 1) using a conventional optical absorption setup that allows high-quality measurements at room temperature¹⁰. These absorption spectra reveal the distinct light absorption mechanisms that may contribute to the opacity of Bgm and Fp in the lowermost mantle. Intervalence Fe²⁺-Fe³⁺ charge transfer (CT) gives rise to the broad absorption band at ~17000 cm⁻¹ in the spectrum of Bgm6 (Mg_{0.94}Fe²⁺_{0.04}Fe³⁺_{0.02}Al_{0.01}Si_{0.99}O₃), which is close in composition to that expected for Bgm in the lower mantle¹¹. Crystal field (*d-d*) bands were not observed in the thin (~6 μm at 117 GPa) and relatively iron-poor sample studied here, as was also the case in the previous high-pressure studies of lower mantle Bgm^{6,12}. The spectrum of Fp13 showed three multiplicity-allowed low spin Fe²⁺ bands. Both Bgm6 and Fp13 have a distinct UV absorption edge, typically assigned to the Fe-O CT (*e.g.* Ref.¹³).

We continued with dynamic experiments in which the samples were heated by a single 1 μs long near-infrared (1070 nm) laser pulse and probed by an ultra-bright broadband pulsed laser (Methods; Extended Data Fig. 2). Thermal radiation emitted off the dynamically-heated samples vanishes in streak camera images within ~10 μs following the arrival of the heating pulse (Extended Data Fig. 3A). Finite-element modeling of time-dependent thermal fluxes in a pulsed laser-heated DAC also indicates that ~10 μs is sufficient to restore sample's temperature back to 300 K, thanks to the high thermal conductivity of diamond¹⁴. Accordingly, the probe pulse train arriving with an interval of 1 μs traverses distinct thermal states and records the spectroscopic information in time domain. The timing of our dynamic experiments also allows extracting room-temperature absorption spectra prior to the arrival of the heating laser and after quenching. The obtained room-temperature spectra are in good agreement with our wide-range spectra (Fig. 1).

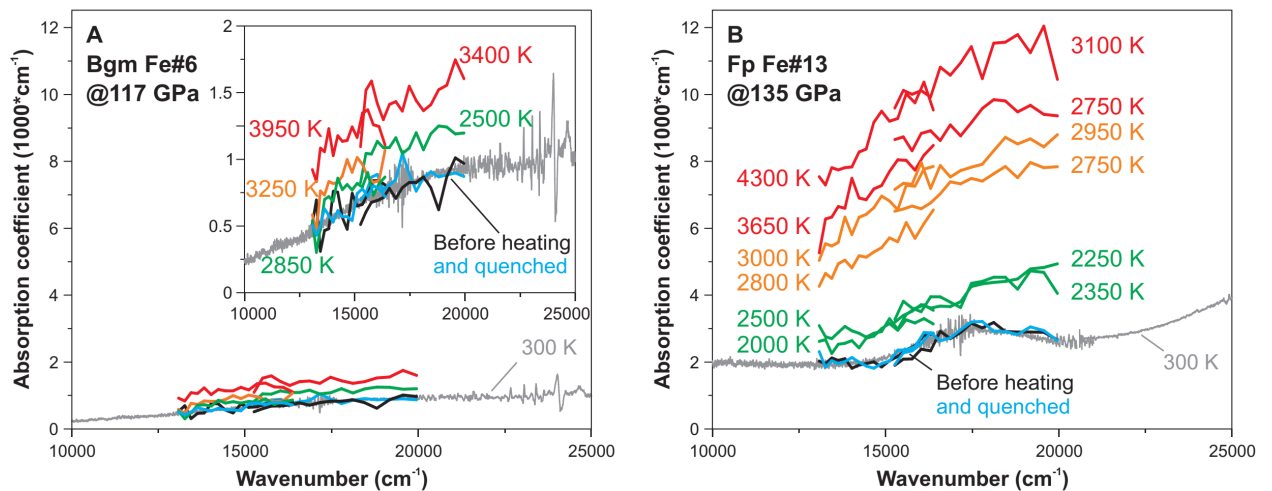


Figure 1. Absorption coefficients of bridgmanite at 117 GPa (A) and ferropericlasite at 135 GPa (B). Black – prior to the heating pulse arrival (1-7 μs); red, orange, or green – upon cooling at high temperature (9-16 μs); and blue – after cooling (20-25 μs). Inset in (A) is a close-up view of Bgm6 data. Temperature uncertainty is ± 500 K. See Methods for details. Grey spectra are absorption coefficients measured prior to heating with a conventional absorption spectroscopy setup (*e.g.* Ref.¹⁰). Corresponding wide-range spectra (SWIR to UV) at 300 K are shown in Extended Data Fig. 1.

Upon heating of Bgm6 to ~2500 K its absorption coefficient (α) averaged over the visible range is enhanced by approximately a factor of two, translating into a relatively small rate of

increase in opacity: $\Delta\alpha/\Delta T$ of $\sim 0.05 \text{ cm}^{-1}/\text{K}$ (Fig. 2). At $T > \sim 3000 \text{ K}$, Bgm6 visible range opacity increases much more rapidly with $\Delta\alpha/\Delta T = 0.4 \text{ cm}^{-1}/\text{K}$, suggesting a crossover to a more efficient light absorption mechanism in Bgm across the temperature range of the TBL. Similarly, the opacity of Fp13 is enhanced at $T > 2000 \text{ K}$ but with a rate that is approximately six times faster than in Bgm6 ($\Delta\alpha/\Delta T = 2.5 \text{ cm}^{-1}/\text{K}$). Specific absorption bands are no longer resolved in the high-temperature spectra of Bgm6 and Fp13 and the visible range opacity is evidently governed by a reversible temperature-induced red-shift of the Fe-O CT (UV absorption edge). Indeed, the initial room-temperature absorption coefficients of Bgm6 and Fp13 are restored after the samples cool down to 300 K. The reversibility in opacity over the heating cycles indicates that our pulsed laser heating time domain experiments probe intrinsic temperature-induced changes in the electronic structure as opposed to extrinsic iron redistribution due to temperature gradients in continuously laser-heated sample.

To gain quantitative information on the opacity of Bgm and Fp at $T < 2000 \text{ K}$ the same DAC loadings were used for static optical absorption experiments in which the samples were continuously laser-heated for 1s and probed by the broadband pulsed laser synchronized with a gated detector (Methods). Heating of Bgm6 to $\sim 2000 \text{ K}$ results in a slight decrease of its Fe^{2+} - Fe^{3+} CT band intensity while the contribution of the UV absorption edge is enhanced (Extended Data Fig. 4). This static experiment reveals the competing of individual light absorption mechanisms in Bgm6 at $T < 2000 \text{ K}$, which is the cause of the relatively small net increase of its opacity in its temperature range ($\Delta\alpha/\Delta T = 0.05 \text{ cm}^{-1}/\text{K}$), in excellent agreement with the rate inferred from the dynamic experiments described above (Fig. 2). Unfortunately, in static experiments on Fp13 we could not achieve satisfactory spectra reversibility at $T > 1000 \text{ K}$, which we tentatively assign to Soret-like iron diffusion due to the unavoidable temperature gradients in a laser-heated DAC. Note that the iron diffusivity in Fp is several orders of magnitude higher than in Bgm (*e.g.* Ref.¹⁵). Apparently, the use of a single and short laser-heating pulse in dynamic experiments allowed us to suppress this unwanted irreversible effect.

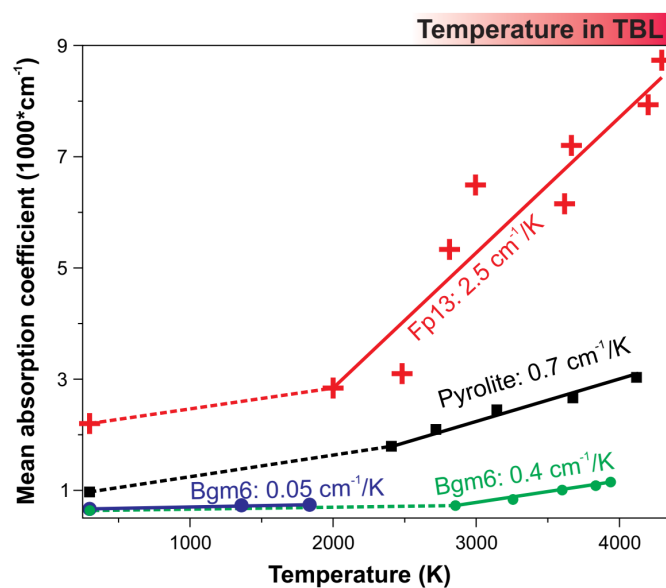


Figure 2. Temperature dependence of the mean absorption coefficients ($13100\text{-}16400 \text{ cm}^{-1}$) observed in dynamic laser-heating experiments on bridgmanite at 117 GPa (Bgm6, green), ferropericlase at 135 GPa (Fp13, red), and pyrolite at 130 GPa (black). Dashed lines show an extrapolation from the 2500-3000 K data to 300 K. The violet

solid line shows the mean absorption coefficient of Bgm6 obtained in static laser-heating experiments. Temperature uncertainty is $\sim \pm 500$ K and $\sim \pm 200$ K in dynamic and static experiments, respectively. The red bar above the figure depicts the temperature increase expected in the thermal boundary layer (TBL).

The crossover in the slope of $\Delta\alpha/\Delta T$ in Bgm and Fp at $T > 2000$ K indicates a transition to the opacity regime dominated by the Fe-O CT, which is centered in the UV and is much more intense than $d-d$ or $\text{Fe}^{2+}\text{-Fe}^{3+}$ transitions because electronic states of different parity (d and p) are involved in the excitation. Thus, the visible range opacity of Bgm and Fp in the lowermost mantle is governed by the Fe-O $p-d$ orbital overlap. Iron in the studied Bgm6 sample is predominantly eightfold-coordinated (distorted pseudododecahedral site)¹¹ while Fp hosts iron exclusively at the octahedral site. The $p-d$ orbital overlap at the sixfold site in Fp is definitely larger than that at the twelvefold site in Bgm by virtue of a shorter Fe-O bond in Fp. As a result, the contribution of the Fe-O CT to the visible range absorbance is stronger in Fp and the corresponding $\Delta\alpha/\Delta T$ (*i.e.* temperature-induced red-shift) is a factor of six higher than in Bgm. Temperature-induced red-shifts of the Fe-O CT band have been identified in many ferromagnesian minerals at relatively low pressure and $T < 1700$ K (*e.g.* Refs.^{13,16,17}), but the effect this mechanism bears on the lower mantle opacity and by extension its transport properties has never been quantified.

To understand the combined effect of Bgm and Fp on the opacity of the lower mantle in a realistic representative composition, we performed dynamic-heating optical experiments on pyrolite at 130 GPa and up to ~ 4000 K (Extended Data Fig. 5). We find that at $T > 2500$ K the absorption coefficient of pyrolite increases with $0.7 \text{ cm}^{-1}/\text{K}$, in excellent agreement with the expectation ($\Delta\alpha/\Delta T = 0.8 \text{ cm}^{-1}/\text{K}$) for a 4:1 mixture of Bgm with Fp, approximating their volume fractions in a pyrolite model (Fig. 2). The derived absolute value of the mean absorption coefficient at 300 K ($\sim 1000 \text{ cm}^{-1}$) for such a pyrolite composition is sensitive to the scattering correction applied to compensate for light scattering on grain boundaries. Here, we estimated the contribution of scattering to the measured light extinction coefficient in pyrolite based on the 300 K absorption coefficients of Bgm6 and Fp13 (Extended Data Fig. 1), which is appropriate because scattering is negligible in single crystals. In any case, the extracted values of $\Delta\alpha/\Delta T$ are robust as they do not depend on the scattering correction, assuming light scattering does not change significantly with T . This assumption is rather accurate as values of $\Delta\alpha/\Delta T$ expected for a mixture of Bgm and Fp based on the single crystal measurements and observed directly in pyrolite are in excellent agreement. Significant grain growth over the $1 \mu\text{s}$ heating cycle, which would affect the scattering at high T , can also be ruled out since the temperature-enhanced absorbance of pyrolite is fully reversible (Extended Data Fig. 5).

In addition to the visible range opacity, we need to constrain the opacity in the near-IR spectra range, where most of the radiative flux is expected at all plausible mantle temperatures. Towards this end, we computed the electronic structure of $(\text{Mg}_{0.875}\text{Fe}_{0.125})\text{O}$ (Methods) at P - T conditions mimicking that in our optical experiments (135 GPa, 4300 K). The computed electronic density of states (DOS) shows a non-zero density of d -electrons at the Fermi level due to the overlapping iron d -orbitals (Extended Data Fig. 6). Local projection of the states identifies the peak centered at -1 eV as the t_{2g} states and the peak centered at $+1$ eV as the e_g states of iron, both mixed with oxygen p states. Electronic excitations between the occupied and unoccupied d and p states give rise to the distinct absorption bands observed at ~ 0.5 and ~ 2 eV (Extended Data

Fig. 7), further supporting the primary role of the Fe-O CT mechanism in the overall opacity of Fp at CMB conditions.

We model radiative thermal conductivity (k_{rad}) in the TBL above the CMB using the experimentally-measured absorption coefficients of Fp and Bgm at 117-135 GPa and 2500-4300 K. The measured absorption coefficients of Fp were extrapolated to 3000 cm^{-1} and 25000 cm^{-1} using a model that allows for a smooth decrease in the absorption coefficient with frequency (Methods, Extended Data Fig. 8A). Using this lower bound constraint on the Fp13 absorption coefficient we can now obtain its radiative thermal conductivity (Methods): $\sim 0.2\text{ W/m/K}$ at 135 GP and 2500-4300 K (Fig. 3A). By extrapolating the absorption coefficients of Bgm6 in a similar fashion (Extended Data Fig. 8B) we obtain a radiative conductivity in the range of $\sim 1.2\text{--}1.4\text{ W/m/K}$ at $T \sim 3000\text{--}4000\text{ K}$ (Fig. 3B). Please note that the obtained k_{rad} values are upper bounds because both Fp and Bgm are expected to show absorption bands in the IR, which we did not take into account in evaluating radiative conductivity.

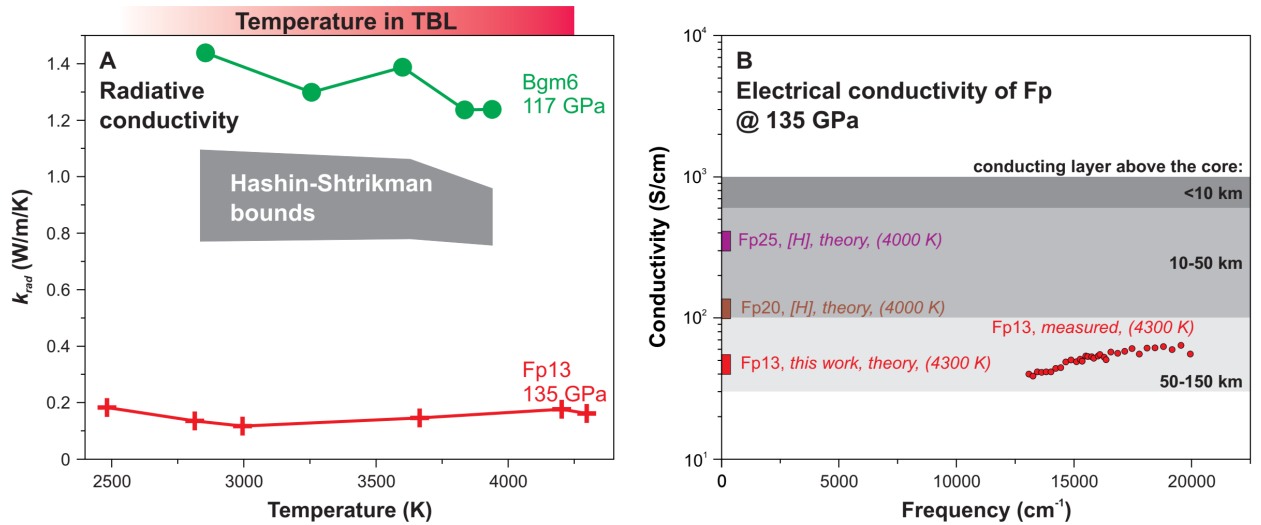


Figure 3. (A) Radiative conductivity of ferropericlase ($\text{Mg}_{0.87}\text{Fe}_{0.13}\text{O}$) and bridgmanite ($\text{Mg}_{0.94}\text{Fe}^{2+}_{0.04}\text{Fe}^{3+}_{0.02}\text{Al}_{0.01}\text{Si}_{0.99}\text{O}_3$) at the P - T conditions of the lowermost mantle. The corresponding Hashin-Shtrikman bounds¹⁸ for a mixture of 80 vol.% Bgm and 20 vol.% Fp are shown in black. The red bar above the figure depicts the temperature increase expected in the thermal boundary layer (TBL). (B) Optical conductivity of ($\text{Mg}_{0.87}\text{Fe}_{0.13}\text{O}$) measured at 135 GPa and 4300 K (red circles) and the corresponding DC electrical conductivity (red rectangle). Values for DC electrical conductivity of Fp with higher iron content from Holmstrom, et al.¹⁹. The grey shaded areas depict the ranges of Fp DC conductivity that would provide a conductance of 10^8 S in the lowermost 10, 10-50, and 50-150 km when mixed with insulating Bgm (0.03 S/cm)²⁰, as required for the core-mantle electromagnetic coupling sufficient to produce the observed 6 year component in the length of day fluctuations^{8,9}.

Interestingly, radiative conductivity of Bgm and Fp at high P - T conditions is essentially temperature-invariant, unlike that of semi-transparent materials where $k_{rad} \sim \frac{T^3}{\alpha(P,T)}$ (Ref.²¹). Evidently, the transfer of radiative energy in the lowermost mantle is diminished by the temperature-induced opacity of Fp and Bgm revealed here. Assuming appropriate volume fractions of Bgm and Fp in the pyrolitic model (0.8 and 0.2) we obtained the Hashin-Shtrikman bounds¹⁸ on the effective radiative conductivity in the lowermost mantle (Fig. 3A). The present results indicate that the radiative conductivity remains largely constant across the TBL and is smaller than $\sim 1\text{ W/m/K}$. The absorption coefficient of post-perovskite is about two times higher than that of Bgm at the total iron content of $\sim 10\text{ mol.}\%$ but shows a qualitatively similar

temperature-dependence of its individual absorption bands²² to that observed in Bgm in this work due to their crystal chemical similarity. Therefore, the inclusion of post-perovskite into the model would result in lower radiative conductivity values.

Our DFT computations also indicate that the electronic contribution to the total thermal conductivity is non-negligible and is ~ 1 W/m/K (Extended Data Fig. 9), which is consistent with the estimate of Holmstrom, et al.¹⁹ for Fp with 19 mol.% Fe. However, the relatively small volume fraction of Fp (20 vol.%) in the lower mantle suggests that the electronic contribution of Fp to the total thermal conductivity of the lowermost mantle is insignificant (~ 0.2 W/m/K). Accordingly, our estimate of the total thermal conductivity of a pyrolitic mantle ($k_{total} = 9-11$ W/m/K) only accounts for the radiative ($k_{rad} = 1$ W/m/K, this work) and lattice contributions (8-10 W/m/K at CMB, previous studies²³⁻²⁵). In a homogeneous TBL the heat flow across the CMB is given by the Fourier law of heat conduction (Eq. 1). Accepting an average temperature gradient in TBL of ~ 0.007 K/m²⁶ and our estimate of the total thermal conductivity at the base of the mantle we obtain a Q_{CMB} of 9-11 TW, which is in the range of estimates based on core energetics and mantle dynamics (8-16 TW)³. The apparent invariance of k_{rad} to T found here implies that heat transport by light radiation has remained relatively inefficient throughout geologic time and could not have promoted a higher Q_{CMB} in the hotter ancient Earth.

In addition to the heat transport across the CMB, our results offer a cross-check on the geodesy-based inference of high electrical conductance (10^8 S) layer 10-150 km above the core. Here we showed that Bgm is insulating under near-CMB conditions as it remains relatively transparent in the visible range even at $T \sim 4000$ K; thus, the potentially high DC conductivity of the lowermost mantle cannot be due to Bgm. This is also supported by previous studies that inferred a relatively low Bgm (and post-perovskite) electrical conductivity ($\sim 0.01-0.03$ S/cm) at high P - T conditions (e.g. Ref.^{20,27}). In contrast to Bgm, the measured absorption coefficients of Fp imply that its DC conductivity is much higher than that of Bgm at near CMB conditions. The computed electrical conductivities of $(\text{Mg}_{0.875}, \text{Fe}_{0.125})\text{O}$ at 135 GPa and 4300 K span $\sim 45-165$ S/cm (Extended Data Fig. 10), depending mainly on the band gap correction used in the computation. This result is not only consistent with the recent theoretical estimates¹⁹, but it falls within the range of DC conductivities required to produce the conductance of 10^8 S in a 50-150 km thick mixture of insulating Bgm (80 vol.%) with conducting Fp (20 vol.%) (Fig. 3B). The necessary electrical conductance may be achieved even in a thin (e.g. < 50 km) layer just above the core if the electrical conductivity of Fp is greater than 100 S/cm. The results of this work together with previous first-principles computations¹⁹ are consistent with such high electrical conductivity in iron-enriched Fp (> 20 mol.% Fe), which could be a plausible explanation for the six year oscillation in the length of day^{8,9}. Seismic tomography images have revealed patches of ULVZs that could be explained by the occurrence of iron-enriched Fp (e.g. Ref.²⁸). If such, these regions implement strongest core-mantle electromagnetic coupling and may manifest themselves in geomagnetic features observable at the Earth's surface. A large ULVZ located beneath the Central Pacific may electromagnetically screen the varying field of the core^{1,2}, which would explain the anomalously low geomagnetic secular variations observed in this region at least over the past 10-100 Ka (e.g. Refs.^{29,30}). Likewise, electric currents in a ULVZ triggered by rapid changes in the orientation of the magnetic dipole during geomagnetic reversals may generate a torque on the core and guide the reversing dipole along the meridians that border the ULVZ (e.g.

Refs.^{1,2}). Therefore, the preference of reversal paths that border the Pacific Ocean may be due to the ULVZ detected beneath the Pacific.

Overall, our results underscore the link between radiative and electrical conductivity. Moderately opaque and electrically insulating Bgm has small but non-negligible radiative thermal conductivity the magnitude of which determines the radiative heat flux in the lowermost mantle. Highly opaque Fp has negligible radiative thermal conductivity but its semi-metallic electrical conductivity is sufficient to implement efficient core-mantle electromagnetic coupling. Therefore, possible variations in the mineralogical abundances of these minerals along the CMB (*e.g.* in the basaltic and pyrolitic compositions) provide the means for heterogeneous CMB thermal and electromagnetic interaction. Strongest core-mantle electromagnetic interaction is expected in regions where Fp is present at the CMB, which may be detected in the secular signal of Earth's magnetic field.

Acknowledgements

The authors thank T. Okuchi and N. Purevjav in synthesis of Fp and Bgm samples. SSL acknowledges the support of the Helmholtz Young Investigators Group CLEAR (VH-NG-1325). FS was supported by a Marie Skłodowska-Curie action under the project ABISSE (grant agreement no. 750901). The work at Carnegie was supported by the NSF (grant numbers DMR-1039807, EAR-1520648, EAR/IF-1128867, and EAR-1763287), the Army Research Office (grant 56122-CH-H), the Deep Carbon Observatory, and the Carnegie Institution of Washington. Numerical simulations were performed on the GENCI supercomputer Occigen through the stl2816 series of eDARI computing grants. JFL acknowledges support by the NSF Geophysics Program (EAR-1446946 and EAR-1916941). JB acknowledges support by IPGP multidisciplinary program PARI, by Region Île de France SESAME Grant no. 12015908, and by Université de Paris UnivEarthS Labex program (ANR-10-LABX-0023 and ANR-11-IDEX-0005-02).

References

- 1 Runcorn, S. K. Polar Path in Geomagnetic Reversals. *Nature* **356**, 654-656 (1992).
- 2 Buffett, B. A. in *Treatise on Geophysics (Second Edition)* (ed Gerald Schubert) 213-224 (Elsevier, 2015).
- 3 Lay, T., Hernlund, J. & Buffett, B. A. Core-mantle boundary heat flow. *Nat. Geosci.* **1**, 25-32 (2008).
- 4 Garnero, E. J. & McNamara, A. K. Structure and dynamics of Earth's lower mantle. *Science* **320**, 626-628 (2008).
- 5 Goncharov, A. F., Haugen, B. D., Struzhkin, V. V., Beck, P. & Jacobsen, S. D. Radiative conductivity in the Earth's lower mantle. *Nature* **456**, 231-234 (2008).
- 6 Keppler, H., Dubrovinsky, L. S., Narygina, O. & Kantor, I. Optical absorption and radiative thermal conductivity of silicate perovskite to 125 Gigapascals. *Science* **322**, 1529-1532 (2008).
- 7 Nimmo, F. in *Treatise on Geophysics (Second Edition)* (ed Gerald Schubert) 27-55 (Elsevier, 2015).
- 8 Holme, R. & de Viron, O. Characterization and implications of intradecadal variations in length of day. *Nature* **499**, 202-205 (2013).
- 9 Buffett, B. A. Constraints on Magnetic Energy and Mantle Conductivity from the Forced Nutations of the Earth. *J. Geophys. Res. Solid Earth* **97**, 19581-19597 (1992).

- 10 Goncharov, A. F., Beck, P., Struzhkin, V. V., Haugen, B. D. & Jacobsen, S. D. Thermal conductivity of lower-mantle minerals. *Phys. Earth Planet. Inter.* **174**, 24-32 (2009).
- 11 Mao, Z. *et al.* Equation of state and hyperfine parameters of high-spin bridgmanite in the Earth's lower mantle by synchrotron X-ray diffraction and Mossbauer spectroscopy. *Am. Mineral.* **102**, 357-368 (2017).
- 12 Goncharov, A. F. *et al.* Experimental study of thermal conductivity at high pressures: Implications for the deep Earth's interior. *Phys. Earth Planet. Inter.* **247**, 11-16 (2015).
- 13 Burns, R. G. *Mineralogical applications of crystal field theory*. 2nd edn, (Cambridge University Press, 1993).
- 14 Montoya, J. A. & Goncharov, A. F. Finite element calculations of the time dependent thermal fluxes in the laser-heated diamond anvil cell. *J. Appl. Phys.* **111**, 112617 (2012).
- 15 Ammann, M. W., Brodholt, J. P. & Dobson, D. P. Ferrous iron diffusion in ferro-periclase across the spin transition. **302**, 393-402 (2011).
- 16 Shankland, T. J., Nitsan, U. & Duba, A. G. Optical absorption and radiative heat transport in olivine at high temperature. *J. Geophys. Res.* **84**, 1603-1610 (1979).
- 17 Lobanov, S. S., Holtgrewe, N. & Goncharov, A. F. Reduced radiative conductivity of low spin FeO₆-octahedra in FeCO₃ at high pressure and temperature. *Earth Planet. Sci. Lett.* **449**, 20-25 (2016).
- 18 Hashin, Z. & Shtrikman, S. A variational approach to theory of effective magnetic permeability of multiphase materials. *J. Appl. Phys.* **33**, 3125-3131 (1962).
- 19 Holmstrom, E., Stixrude, L., Scipioni, R. & Foster, A. S. Electronic conductivity of solid and liquid (Mg, Fe)O computed from first principles. *Earth Planet. Sci. Lett.* **490**, 11-19 (2018).
- 20 Sinmyo, R., Pesce, G., Greenberg, E., McCammon, C. & Dubrovinsky, L. Lower mantle electrical conductivity based on measurements of Al, Fe-bearing perovskite under lower mantle conditions. *Earth Planet. Sci. Lett.* **393**, 165-172 (2014).
- 21 Clark, S. P. Radiative transfer in the Earth's mantle. *Eos (formerly Trans. Am. Geophys. Union)* **38**, 931-938 (1957).
- 22 Lobanov, S. S., Holtgrewe, N., Lin, J. F. & Goncharov, A. F. Radiative conductivity and abundance of post-perovskite in the lowermost mantle. *Earth Planet. Sci. Lett.* **479**, 43-49 (2017).
- 23 Ohta, K., Yagi, T., Hirose, K. & Ohishi, Y. Thermal conductivity of ferropericlase in the Earth's lower mantle. *Earth Planet. Sci. Lett.* **465**, 29-37 (2017).
- 24 Okuda, Y. *et al.* The effect of iron and aluminum incorporation on lattice thermal conductivity of bridgmanite at the Earth's lower mantle. *Earth Planet. Sci. Lett.* **474**, 25-31 (2017).
- 25 Hsieh, W. P., Deschamps, F., Okuchi, T. & Lin, J. F. Effects of iron on the lattice thermal conductivity of Earth's deep mantle and implications for mantle dynamics. *Proc. Natl. Acad. Sci. U.S.A.* **115**, 4099-4104 (2018).
- 26 Stacey, F. D. & Davis, P. M. *Physics of the Earth*. 4th edn, (Cambridge University Press, 2008).
- 27 Ohta, K. *et al.* The electrical conductivity of post-perovskite in Earth's D" layer. *Science* **320**, 89-91 (2008).
- 28 Wicks, J. K., Jackson, J. M., Sturhahn, W. & Zhang, D. Z. Sound velocity and density of magnesiowustites: Implications for ultralow-velocity zone topography. *Geophys. Res. Lett.* **44**, 2148-2158 (2017).
- 29 Constable, C., Korte, M. & Panovska, S. Persistent high paleosecular variation activity in southern hemisphere for at least 10 000 years. *Earth Planet. Sci. Lett.* **453**, 78-86 (2016).
- 30 Panovska, S., Constable, C. G. & Korte, M. Extending Global Continuous Geomagnetic Field Reconstructions on Timescales Beyond Human Civilization. *Geochem. Geophys. Geosys.* **19**, 4757-4772 (2018).

1 **Extended Data and Methods**

2 **Diamond anvil cell and sample assembly**

3 Rhenium gaskets were indented by compression to a pressure of ~30 GPa in diamond
4 anvil cells equipped with beveled anvils having 100/300 and 80/300 μm culets. Subsequently,
5 circular holes with a diameter of ~50 μm were laser-drilled in the center of the indentation to
6 serve as sample containers. After the drilling, the gaskets were washed in isopropanol for 30 min
7 and mounted between the diamond anvils. Prior to positioning the sample, wafers of dry KCl (5
8 μm thick) were centered on each of the anvil. Next, double-polished single crystals of
9 ferropericlaite ($\text{Mg}_{0.87}\text{Fe}_{0.13}\text{O}$) and bridgmanite ($\text{Mg}_{0.94}\text{Fe}^{2+}_{0.04}\text{Fe}^{3+}_{0.02}\text{Al}_{0.01}\text{Si}_{0.99}\text{O}_3$) with initial
10 thickness of ~8-10 μm were put into the sample cavity such that a sufficient area of the sample
11 cavity was not covered by the sample to allow for reference transmission measurements through
12 KCl (Extended Data Fig. 2A). Finally, the cells were brought to a desired pressure as gauged
13 either by the position of the diamond Raman edge³¹ or ruby fluorescence³². A typical
14 discrepancy between these reading yields an ambiguity in the pressure estimate of < 5 %. No
15 correction for thermal pressure was applied since added thermal pressure is smaller than 5 GPa at
16 3000 K^{33,34}.

17 **Static optical measurements at high pressure and 300 K**

18 Here we used a custom-built all-reflective microscope combined with an IR, VIS, and
19 near-UV conventional (non-laser) light sources. For the visible and near-UV range we used a
20 fiber-coupled halogen-D₂ lamp focused to a ~50 μm spot on the sample. The transmitted portion
21 of the radiation was collimated by a 20 μm pinhole and sent to the spectrograph (Acton Research
22 Corporation SpectraPro 500-i) equipped with a 300 grooves/mm grating and a CCD chilled to
23 235 K. Measurements in the IR range were performed on the same optical bench but with a
24 Fourier transform spectrometer equipped with a quartz beamsplitter (Varian Resolution Pro 670-
25 IR). Details of our IR-VIS-UV setup have been reported in our previous publications^{10,12,35,36}.
26 Overall, this setup allows for a high-quality absorption spectrum in a wide spectral range (2500-
27 30000 cm^{-1}) at room temperature. Absorption coefficient was evaluated as $\alpha(\nu) = \ln(10) * \frac{1}{d} *$
28 $(- \log_{10}(I_{\text{sample}} - I_{\text{bckg}}) / (I_{\text{reference}} - I_{\text{bckg}}))$, where d is sample thickness at high pressure,
29 I_{sample} is the intensity of light transmitted through the sample, $I_{\text{reference}}$ is the intensity of light
30 passed through the KCl pressure medium, and I_{bckg} is the background reading. Light losses due to
31 the reflections at the sample-KCl interfaces are small (< 1 %) due to the similarity of the KCl
32 and samples' refractive index at $P > 100$ GPa ($n \sim 2$) and were not taken into account.

33 **Static optical measurements at high pressure at $T < \sim 2000$ K**

34 Overall, static optical measurements at continuous laser heating allows probing the
35 sample by a large number of probe pulses, which improves the quality of the resulting absorption
36 spectra as compared to spectroscopic measurements in dynamic experiments (see below).

37 The setup combines a quasi-continuous Yt-doped 1070 nm fiber laser, a pulsed Leukos
38 Pegasus ultra-bright supercontinuum (broadband, ~4000-25000 cm^{-1}) probe operating at 1 MHz,
39 and an intensified gated CCD detector (Andor iStar SR-303i-A). The confocal probe spot size
40 (~5 μm) was smaller than the heating laser spot (~15 μm). The spectral collection was initiated

41 500 ms after the start of a 1 s laser heating cycle. The detector gates were modulated for 200 ms
 42 at a rate of ~ 41 kHz and synchronized with the probe pulses (4 ns pulse width). Probe brightness
 43 was maximized to achieve maximum signal through the reference KCl without saturating the
 44 detector. The precise synchronization of the probe pulses and detector gates diminishes thermal
 45 background, drastically improves the signal-to-background ratio, and allows optical absorbance
 46 measurements in the VIS range (~ 13000 - 22500 cm^{-1}) up to ~ 2000 K. High-temperature
 47 absorption coefficients were evaluated as $\alpha(\nu) = \ln(10) * \frac{1}{d} * (-\log_{10}(I_{sample}^T - I_{bckg}^T) / (I_{reference} - I_{bckg}))$, where I_{sample}^T and I_{bckg}^T are the probe and
 48 background intensity at high temperature. Temperature was measured from both sides of the
 49 sample by imaging the hot spot onto the iCCD detector array. Further details of this setup can be
 50 in Lobanov, et al. ¹⁷.

52 **Dynamic optical measurements at high pressure and $T > \sim 2000$ K**

53 This setup combines the same heating and probe lasers (see above) but spectral
 54 measurements were performed by a Sydor ROSS 1000 streak on a Princeton Instruments
 55 spectrometer (f/4, 150 grooves/mm). Together these components enable single-pulse laser
 56 heating experiments coupled with *in situ* time-resolved absorption measurements at $T > \sim 2000$
 57 K³⁷. Typical streak camera sweeps were 25-30 μs long and, accordingly, recorded 25-30 probe
 58 pulses each of which can be used for spectra evaluation. Importantly, spectral features and
 59 intensity of individual supercontinuum pulses are sufficiently reproducible to allow for single
 60 pulse spectroscopy (as is shown in this work). After initiation of the streak camera image
 61 collection, a single 1 μs long pulse of the 1070 nm fiber laser arrives at the 8th μs to heat the
 62 sample (Extended Data Fig. 2B), allowing for a sufficient number of probe pulses to traverse the
 63 sample prior to heating. Sample absorption at high temperature was recorded by the streak
 64 camera images taken at two distinct grating positions centered at 700 and 590 nm, accessing
 65 15000-20000 and 13000-16400 cm^{-1} spectral ranges, respectively. From streak camera images
 66 the absorption coefficient was evaluated as: $\alpha(\nu) = \ln(10) * \frac{1}{d} * (-\log_{10}(I_{sample}^{time} - I_{bckg}^{time}) / (I_{reference} - I_{bckg}))$, where I_{sample}^{time} and I_{bckg}^{time} are the probe intensity
 67 at a given time and the corresponding (thermal) background. Similarly to the static optical
 68 experiments, reflection losses were unimportant.

70 Overlapping absorption spectra were stitched together to produce a spectrum in the
 71 13000-20000 cm^{-1} range (e.g. Fig. 1). Immediately after the collection of streak camera images
 72 the probe laser was blocked and streak camera images were measured again at identical laser
 73 heating power. These latter images were used to infer the temperature evolution of the sample
 74 for a given laser heating power. In addition, the images of clean thermal background were used
 75 to obtain I_{bckg}^{time} . Temperature measurements at the 700 and 590 nm grating position generally
 76 yielded consistent results. To assign temperatures to stitched spectra we relied on radiometry
 77 measurements with the grating centered at 700 nm, as more light was available for Planck fitting.
 78 However, we could only observe sufficiently intense thermal background (> 10 counts in a single
 79 streak camera sweep) at $T > \sim 3000$ K. To characterize sample absorbencies at lower
 80 temperatures, up to 100 consecutive streak camera sweeps were accumulated at low laser heating
 81 power to improve the statistics, assuming that the coupling of the sample to the heating laser did

82 not change substantially over the 100 heating cycles. In these cases, the sample absorbance was
83 checked afterwards to ensure its full reversibility over the heating cycles.

84 We estimate the overall temperature uncertainty based on the reproducibility of the
85 absorption coefficients at high temperatures. At $T > 2000$ K, the reproducibility of the absorption
86 coefficients was typically within 0-20 %, which translates to the overall ambiguity in the
87 temperature measurements of $< \pm 500$ K. This estimate is independently confirmed by optical
88 observations of dark spots (presumably Fe-rich and formed upon melting) and increased room-
89 temperature absorbencies in samples quenched from temperatures exceeding their expected
90 solidus.

91 **Sample thickness measurements**

92 The thickness of all studied samples was measured *ex situ* after decompression using a
93 Zygo NewView 5032 optical 3D profilometer, which allows imaging of the surface roughness at
94 an extremely high precision of ~ 10 nm. Samples were carefully extracted out of the DAC,
95 positioned on a clean glass slide, washed with distilled water to dissolve KCl, and then brought
96 in for Zygo imaging (Extended Data Fig. 11). The thickness at high pressure was reconstructed
97 using the equations of state of bridgmanite (MgSiO_3) and periclase (MgO) assuming a perfectly
98 elastic sample behavior upon decompression. The use of iron-free endmembers is adequate as
99 the differences in compressibility contribute a negligibly small systematic uncertainty of < 0.2 %
100 to the reconstructed thickness at $P \sim 117$ -135 GPa.

101 **Radiative conductivity evaluation and Smith-Drude fitting**

102 Under the assumption that the grain size is substantially larger than the photon mean free
103 path the radiative conductivity of an absorbing medium is given by²¹: $k_{rad}(T) =$
104 $\frac{4n^2}{3} \int_0^\infty \frac{1}{\alpha(\nu)} \frac{\partial I(\nu, T)}{\partial T} d\nu$ (Eq. 2), where $\alpha(\nu)$ is the frequency-dependent absorption coefficient of the
105 medium, n its refractive index, and $I(\nu, T)$ is the Planck function. At $T = 3000$ -4000 K, the visible
106 light photon mean free path ($1/\alpha$) in Bgm and Fp is < 10 μm (Fig. 1). Accordingly, we assume
107 that the grain size in the proximity of the core-mantle boundary is larger than 10 μm . We note
108 that while this has been a typical assumption made in previous studies of lower mantle k_{rad} ^{5,6,12},
109 independent estimates of the grain size in the bulk lower mantle point towards 100-1000 μm
110 grain size³⁸; thus, validating Eq. 2.

111 Accurate estimates of radiative conductivity require that the frequency-dependence of the
112 absorption coefficient is known in a wide spectral range (e.g. 3000-25000 cm^{-1}). In the case of
113 Fp, we used the Smith-Drude model³⁹ to extrapolate the experimental data into the IR range.
114 Smith-Drude model only gives the lower limit on the absorption coefficient in the IR, as it does
115 not account for $d-d$ transitions, which are expected in the IR based on our theoretical
116 computations of the Fp absorption spectrum. The following procedure was used to obtain Smith-
117 Drude fits. First, the measured absorption coefficients ($P = 135$ GPa, $T = 2500$ -4300 K) were
118 converted to optical conductivity: $\sigma = n * \alpha * c * \epsilon_0$, where n is refractive index (~ 2), c is the
119 speed of light, and ϵ_0 is the permittivity of free space, which was then fit to the Smith-Drude
120 model (with the c model parameter fixed to -1, in order to gain the lowest possible values of
121 optical conductivity in the IR). The obtained Smith-Drude optical conductivities were then
122 converted back into the absorption coefficients (3000-25000 cm^{-1} spectral range) and used to

123 evaluate radiative conductivity at the given P - T conditions. **Extended Data Fig. 8A** shows the
124 results of the Smith-Drude fit to the ferropericlase experimental data at 135 GPa.

125 In the case of Bgm, the experimentally measured absorption spectra were also
126 extrapolated using the Smith-Drude approach outlined above. Crystal field (d - d) transition are
127 expected to be important in the IR range due to the large Fe-O distance at the dodecahedral site
128 that results in a d - d absorption band centered at ~ 7000 cm^{-1} (1 atm, 300 K)⁴⁰. Accordingly, we
129 again expect the Smith-Drude approach to underestimate the absorption coefficient in the IR.
130 **Extended Data Fig. 8B** shows the results of the Smith-Drude fit to the experimental data on
131 bridgmanite at 117 GPa. We also tested an alternative approach to estimate the absorption
132 coefficient of Bgm in the IR that is based on the measured rates of changes in its absorption
133 coefficient with temperature in the visible range. Here we assume a linear and frequency-
134 independent increase in the absorption coefficient of 0.05 and 0.4 cm^{-1} at 300-3000 K and 3000-
135 4000 K (**Fig. 2**), respectively. This approach always yields higher absorption coefficients in the
136 IR than the Smith-Drude approach. However, the difference in resulting Bgm k_{rad} values is
137 relatively small: ~ 20 %. For the purpose of constraining the upper limit on k_{rad} (**Fig. 3A**) we only
138 used the Smith-Drude models to infer radiative conductivity.

139 **First-principles computations**

140 We used *ab initio* simulations to study the electronic structure of Fp and to determine the
141 behavior of the dynamical electrical conductivity. We performed molecular dynamics of
142 $(\text{Mg}_{0.875}\text{Fe}_{0.125})\text{O}$ coupled to density functional theory at finite temperature in the Mermin Kohn-
143 Sham scheme^{41,42} using the VASP Package⁴³. The cell was composed of 28 magnesium atoms, 4
144 iron and 32 oxygen. We used a cubic cell with periodic boundary conditions to limit the finite
145 size effects. We placed the atoms in a B1 structure with the iron atoms placed in lieu of
146 magnesium atoms. The density was set to 5.48 g/cm^3 . The temperature was controlled by a Nosé
147 thermostat^{44,45} and set to 4300 K. We used a time-step of 0.5 fs for a total duration of 7 ps. For
148 the DFT calculation, we used projector augmented wave pseudo-potentials⁴⁶ with hard cut-offs
149 but a frozen core of $1s^2$ for Mg and O, and $1s^2 2s^2 2p^6 3s^2$ for iron. The energy cut-off was set to
150 1200 eV. We used a Fermi-Dirac distribution to populate the electronic eigenstates. We sampled
151 the Brillouin zone with the Γ -point only as it was sufficient for the trajectory. To determine the
152 detailed electronic structure and the transport properties, we performed additional calculations on
153 snapshots taken every 500 timestep. We used the package Abinit⁴⁷ with 672 bands and 4^3
154 Monkhorst-Pack grid of K-points⁴⁸. We used non spin-polarized calculations as the results were
155 indistinguishable from spin polarized results. We used the linear response theory framework to
156 study the transport properties^{49,50}. We show the results of the absorption coefficient, electrical
157 conductivity, and the electronic contribution to the total thermal conductivity as a function of
158 excitation energy in the **Extended Data Figures 7, 9 and 10**. We performed calculations with the
159 HSE06⁵¹ functional and also with the Hubbard U correction of 2.5 eV as in Holmstrom, et al. ¹⁹.

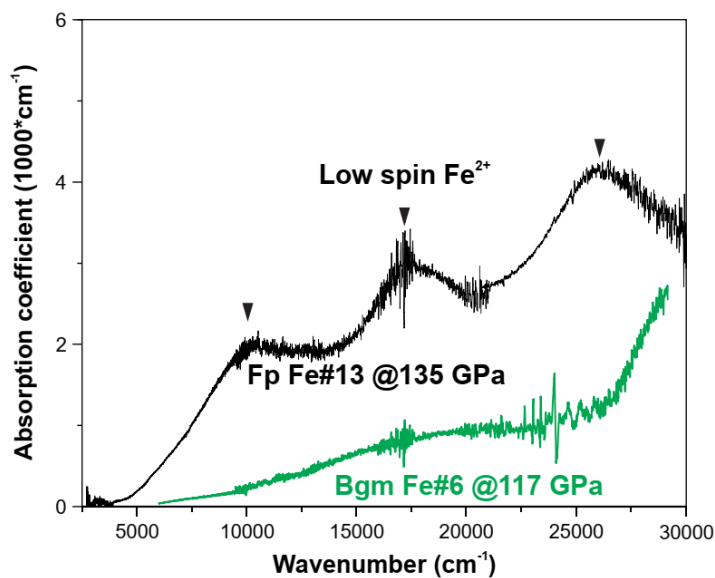
160 Overall, the computed absorption coefficient of Fp at 135 GPa and 4300 K is in
161 qualitative agreement with the experimental measurements on Fp13 but is offset to lower energy
162 and is of a higher magnitude, likely due to the underestimated band gap, which is a known issue
163 of PBE-DFT⁵⁰. In order to correct for the gap underestimation that is common with GGA-DFT,
164 we manually shifted the eigenenergies of the bands above the Fermi level by a fixed value of
165 $+0.5$ or $+1.0$ eV⁵². Nevertheless, this shift is not fully consistent as the Kohn-Sham orbitals are

166 likely to be modified by this operation and this was not taken into account. By rescaling the
 167 magnitude of the absorption coefficient we obtained a decent agreement with the experimental
 168 results as can be seen in [Extended Data Figure 7](#).

169 Regardless of the used corrections, the inference of strongly absorbing Fp in the IR range
 170 is robust as Holmstrom, et al.¹⁹ found largely similar DOS of $(\text{Mg}_{0.75}, \text{Fe}_{0.25})\text{O}$ at comparable P - T
 171 conditions using a DFT methodology that included a Hubbard correction. Also, related orbital
 172 overlaps have been found in FeO at finite temperature using DFT coupled to dynamic mean field
 173 theory (DMFT) calculations⁵³. This similarity indicates that Mg does not prevent the gap closure
 174 in the iron system. It also gives us confidence on the accuracy of our *ab initio* results despite the
 175 lack of DMFT formalism in our case.

176

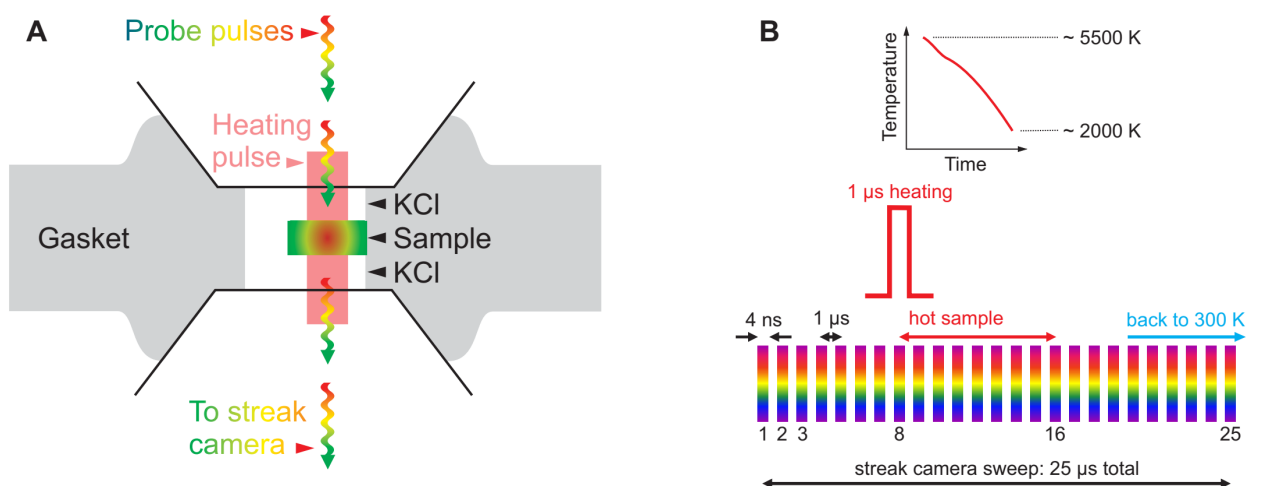
177 **Extended Data Figures**



178

179 **Extended Data Figure 1.** Room-temperature absorption coefficients of Bgm6 (green) and Fp13 (black) at 117 and
 180 135 GPa, respectively, probed by a conventional optical spectroscopy in infrared, visible, and near-ultraviolet
 181 spectral ranges^{10,12}.

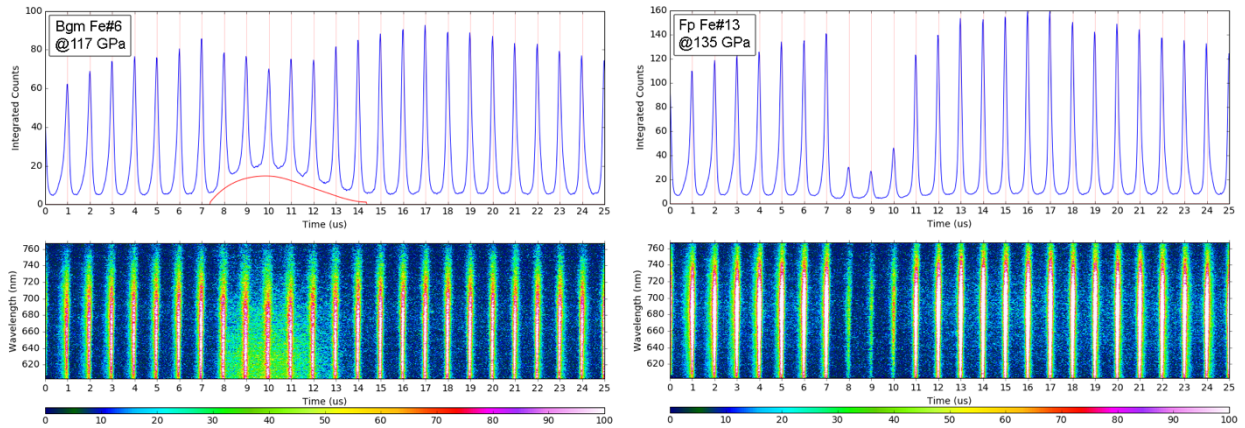
182



183

184 **Extended Data Figure 2.** (A) Diamond anvil cell assemblage used in this work. Samples were sandwiched between
 185 two KCl wafers and positioned in the cavity such that part of it can be used to measure optical reference (through
 186 KCl only). (B) Timing of our single laser-heating shot experiments. Probe pulses (supercontinuum laser) traverse
 187 the sample every 1 μs . The 1 μs heating laser (1070 nm, double-sided) arrives at 8 μs of the 25-30 μs long streak
 188 camera sweep.

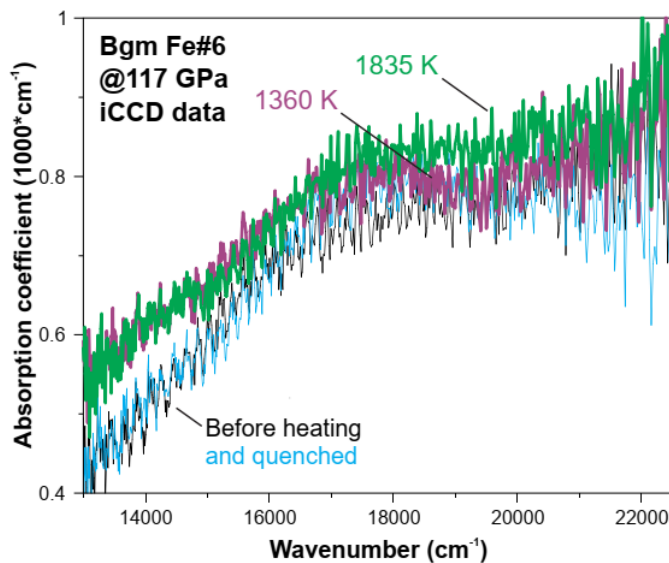
189



190

191 **Extended Data Figure 3.** Representative streak camera images (bottom panels) and corresponding integrated
 192 intensity (top panels) of Bgm6 at 117 GPa (left) and Fp13 at 135 GPa (right). The 1 μs laser heating pulse arrived at
 193 $\sim 8^{\text{th}}$ microsecond heating the samples to a maximum temperature of ~ 4000 K (Bgm) and ~ 3000 K (Fp), in these
 194 particular shots. Note the presence of apparent thermal background in the case of bridgmanite (top panel, red curve).

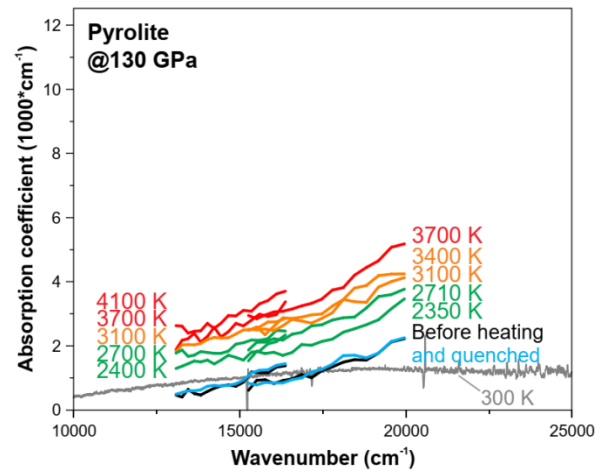
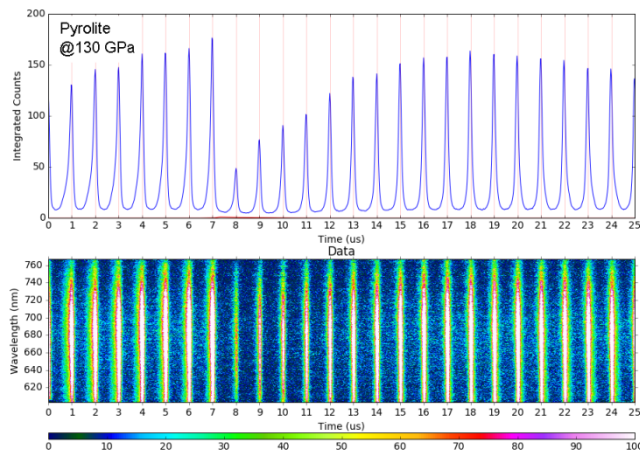
195



196

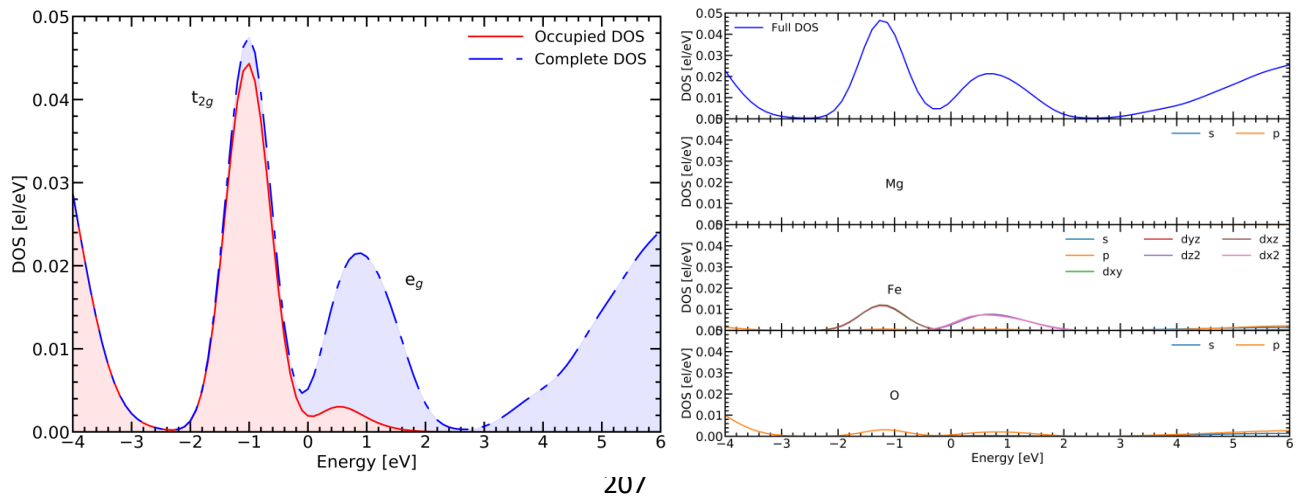
197 **Extended Data Figure 4.** Absorption coefficient of bridgmanite with 6 mol.% Fe at 117 GPa before and
 198 after heating (black and blue), 1360 K (purple), and 1835 K (green). The temperature dependence of the absorption
 199 coefficient is frequency-dependent. Mean absorption coefficient (averaged over the shown spectral) increases with
 200 temperature as $\sim 0.05 \text{ cm}^{-1}/\text{K}$. Detailed description of the used experimental setup is provided in Ref.¹⁷.

201



202

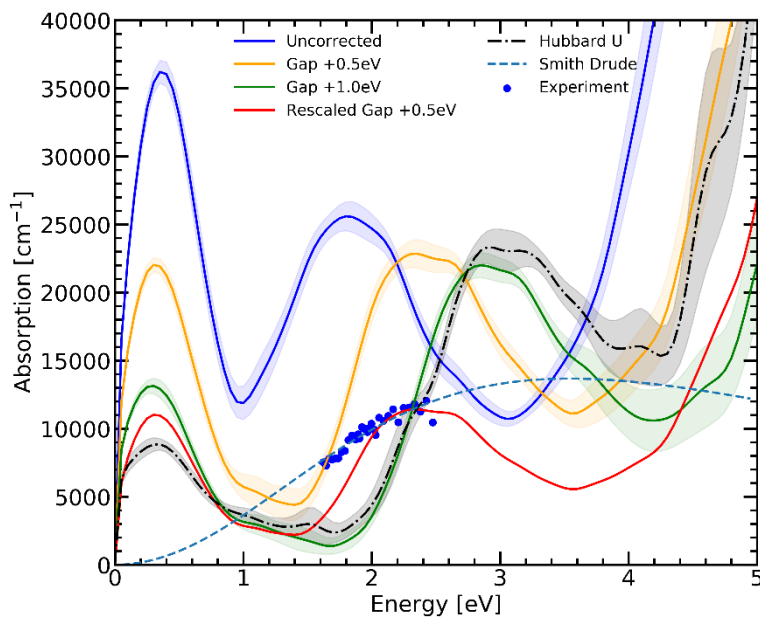
203 **Extended Data Figure 5.** Left: A streak camera image (bottom panel) and the corresponding integrated intensity
 204 (top panel) of pyrolite at 130 GPa. Right: Temperature-dependence of pyrolite absorption coefficients at 130 GPa
 205 (after applying scattering correction based on the 300 K absorption coefficients of Bgm6 at 117 GPa and Fp13 at
 206 135 GPa).



207

208 **Extended Data Figure 6.** Electronic density of states of 12.5 mol.% Fp at 135 GPa and 4300 K. The Fermi level is
 209 at 0 eV. Left: The blue curve is the complete DOS and the red one is the occupied DOS of Fe. Right: Element-
 210 projected DOS.

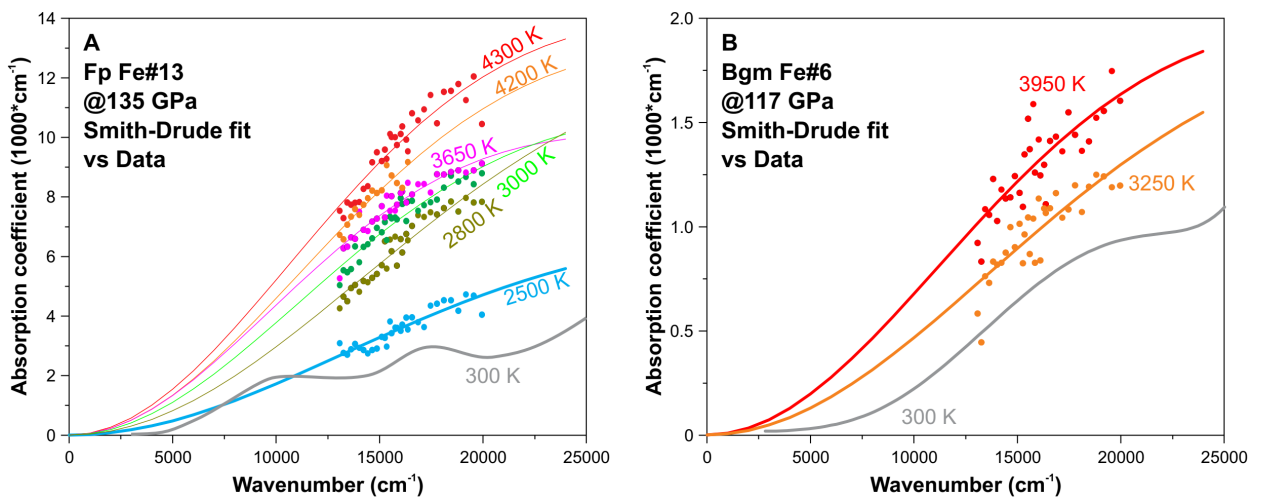
211



212

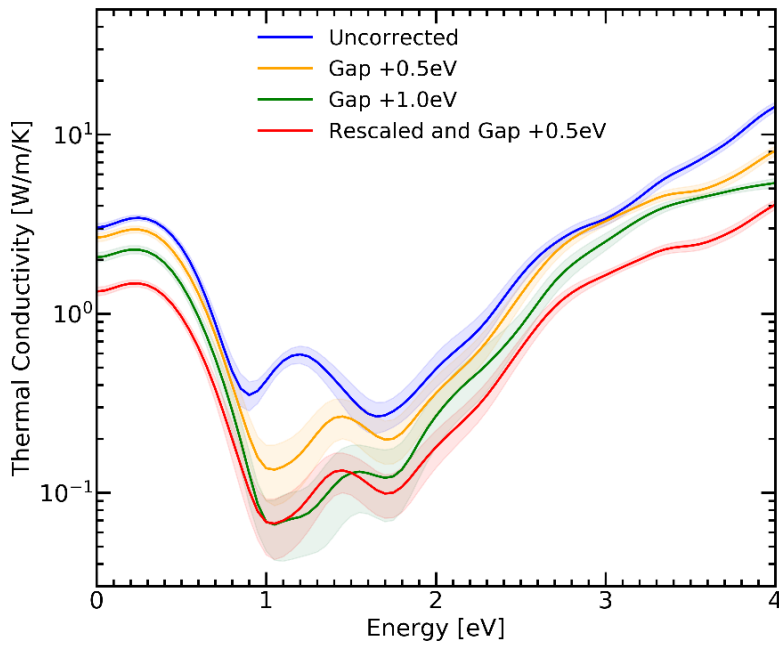
213 **Extended Data Figure 7.** Absorption coefficient of 12.5 mol.% Fp at 135 GPa and 4300 K as a function of the
 214 excitation energy. The blue curve is the direct result from Abinit. The orange and green curves are the results for the
 215 opened energy gap (up to 1 eV). The red curve is the +0.5eV gap rescaled by a factor of 0.5. The blue dots are the
 216 experimental results reported in Fig. 1B. The dashed line is a Smith-Drude fit to the experimental results.

217



218

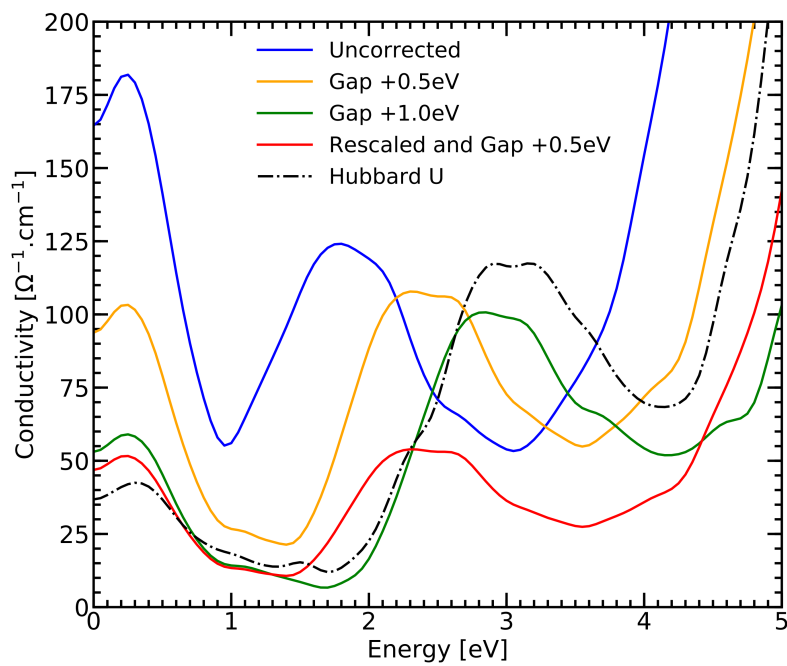
219 **Extended Data Figure 8.** Representative absorption coefficients of ferropericlasite at 135 GPa (A) and bridgmanite
 220 at 117 GPa (B) as a function of temperature (circles, color-coded for temperature). Colored lines are Smith-Drude
 221 fits to the measured data. Grey lines are fits to wide spectral range absorption spectra measured at 300 K.



222

223 **Extended Data Figure 9.** Electronic contribution to the thermal conductivity of 12.5 mol.% Fp at 135 GPa and
 224 4300 K as a function of frequency. The legend is similar to [Extended Data Fig. 7](#).

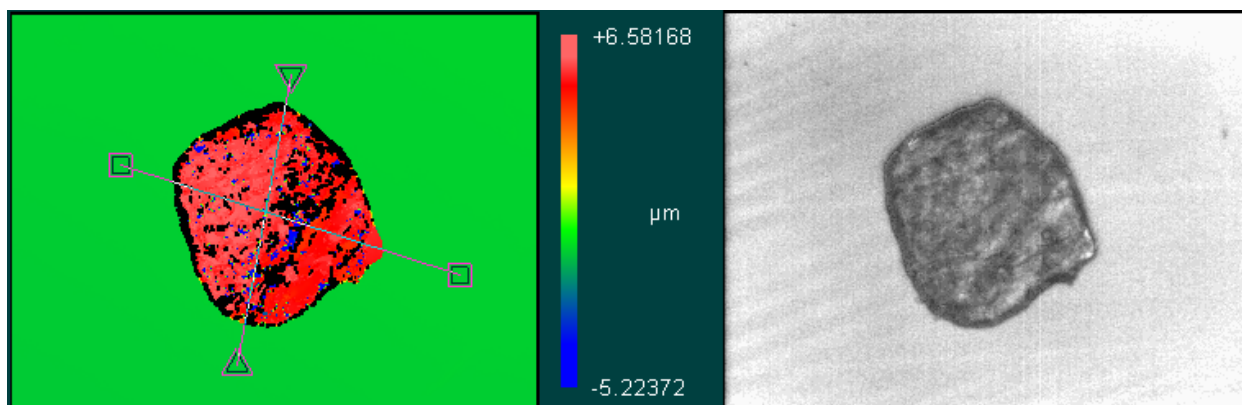
225



226

227 **Extended Data Figure10.** Electrical conductivity of 12.5 mol.% Fp at 135 GPa and 4300 K as a function of the
 228 excitation energy. The legend is similar to [Extended Data Fig. 7](#).

229



230

231 **Extended Data Figure 11.** ZYGO imaging of the bridgmanite sample used in this work after decompression from
 232 117 GPa. The apparent thickness at 1 atm is 6.2 μm. **Left:** Thickness map. **Right:** Intensity map.

233

234 **Extended References**

- 235 5 Goncharov, A. F., Haugen, B. D., Struzhkin, V. V., Beck, P. & Jacobsen, S. D. Radiative conductivity
 236 in the Earth's lower mantle. *Nature* **456**, 231-234 (2008).
- 237 6 Keppler, H., Dubrovinsky, L. S., Narygina, O. & Kantor, I. Optical absorption and radiative thermal
 238 conductivity of silicate perovskite to 125 Gigapascals. *Science* **322**, 1529-1532 (2008).
- 239 10 Goncharov, A. F., Beck, P., Struzhkin, V. V., Haugen, B. D. & Jacobsen, S. D. Thermal conductivity
 240 of lower-mantle minerals. *Phys. Earth Planet. Inter.* **174**, 24-32 (2009).
- 241 12 Goncharov, A. F. *et al.* Experimental study of thermal conductivity at high pressures:
 242 Implications for the deep Earth's interior. *Phys. Earth Planet. Inter.* **247**, 11-16 (2015).
- 243 17 Lobanov, S. S., Holtgrewe, N. & Goncharov, A. F. Reduced radiative conductivity of low spin
 244 FeO₆-octahedra in FeCO₃ at high pressure and temperature. *Earth Planet. Sci. Lett.* **449**, 20-25
 245 (2016).
- 246 19 Holmstrom, E., Stixrude, L., Scipioni, R. & Foster, A. S. Electronic conductivity of solid and liquid
 247 (Mg, Fe)O computed from first principles. *Earth Planet. Sci. Lett.* **490**, 11-19 (2018).
- 248 21 Clark, S. P. Radiative transfer in the Earth's mantle. *Eos (formerly Trans. Am. Geophys. Union)* **38**,
 249 931-938 (1957).
- 250 31 Akahama, Y. & Kawamura, H. Pressure calibration of diamond anvil Raman gauge to 310 GPa. *J.*
 251 *Appl. Phys.* **100**, 043516 (2006).
- 252 32 Syassen, K. Ruby under pressure. *High Pressure Res.* **28**, 75-126 (2008).
- 253 33 Goncharov, A. F. *et al.* Thermal equation of state of cubic boron nitride: Implications for a high-
 254 temperature pressure scale. *Phys. Rev. B* **75**, 224114 (2007).
- 255 34 McWilliams, R. S., Dalton, D. A., Mahmood, M. F. & Goncharov, A. F. Optical Properties of Fluid
 256 Hydrogen at the Transition to a Conducting State. *Phys. Rev. Lett.* **116**, 255501 (2016).
- 257 35 Lobanov, S. S., Goncharov, A. F. & Litasov, K. D. Optical properties of siderite (FeCO₃) across the
 258 spin transition: Crossover to iron-rich carbonates in the lower mantle. *Am. Mineral.* **100**, 1059-
 259 1064 (2015).
- 260 36 Lobanov, S. S., Hsu, H., Lin, J. F., Yoshino, T. & Goncharov, A. F. Optical signatures of low spin
 261 Fe³⁺ in NAL at high pressure. *J. Geophys. Res.* **122**, 3565-3573 (2017).
- 262 37 Jiang, S. Q. *et al.* Metallization and molecular dissociation of dense fluid nitrogen. *Nat. Commun.*
 263 **9**, 2624 (2018).
- 264 38 Solomatov, V. S., El-Khozondar, R. & Tikare, V. Grain size in the lower mantle: constraints from
 265 numerical modeling of grain growth in two-phase systems. *Phys. Earth Planet. Inter.* **129**, 265-
 266 282 (2002).
- 267 39 Smith, N. V. Classical generalization of the Drude formula for the optical conductivity. *Phys. Rev.*
 268 *B* **64**, 155106 (2001).

269 40 Keppeler, H., Mccammon, C. A. & Rubie, D. C. Crystal-field and charge-transfer spectra of
 270 (Mg,Fe)SiO₃ perovskite. *Am. Mineral.* **79**, 1215-1218 (1994).
 271 41 Mermin, N. D. Thermal Properties of the Inhomogeneous Electron Gas. *Phys. Rev.* **137**, A1441-
 272 A1443 (1965).
 273 42 Kohn, W. & Sham, L. J. Self-Consistent Equations Including Exchange and Correlation Effects.
 274 *Phys. Rev.* **140**, A1133-A1138 (1965).
 275 43 Kresse, G. & Furthmuller, J. Efficient iterative schemes for ab initio total-energy calculations
 276 using a plane-wave basis set. *Phys. Rev. B* **54**, 11169-11186 (1996).
 277 44 Nosé, S. A unified formulation of the constant temperature molecular dynamics methods. *J.*
 278 *Chem. Phys.* **81**, 511-519 (1984).
 279 45 Nosé, S. Constant Temperature Molecular-Dynamics Methods. *Prog. Theor. Phys. Suppl.* **103**, 1-
 280 46 (1991).
 281 46 Blochl, P. E. Projector augmented-wave method. *Phys. Rev. B* **50**, 17953-17979 (1994).
 282 47 Gonze, X. *et al.* ABINIT: First-principles approach to material and nanosystem properties.
 283 *Comput Phys Commun* **180**, 2582-2615 (2009).
 284 48 Monkhorst, H. J. & Pack, J. D. Special Points for Brillouin-Zone Integrations. *Phys. Rev. B.* **13**,
 285 5188-5192 (1976).
 286 49 Mazevet, S., Torrent, M., Recoules, V. & Jollet, F. Calculations of the transport properties within
 287 the PAW formalism. *High Energ. Dens. Phys.* **6**, 84-88 (2010).
 288 50 Soubiran, F. & Militzer, B. Electrical conductivity and magnetic dynamos in magma oceans of
 289 Super-Earths. *Nat. Commun.* **9**, 3883 (2018).
 290 51 Heyd, J., Scuseria, G. E. & Ernzerhof, M. Hybrid functionals based on a screened Coulomb
 291 potential. *J. Chem. Phys.* **118**, 8207-8215 (2003).
 292 52 Kowalski, P. M., Mazevet, S., Saumon, D. & Challacombe, M. Equation of state and optical
 293 properties of warm dense helium. *Phys. Rev. B* **76**, 075112 (2007).
 294 53 Ohta, K. *et al.* Experimental and Theoretical Evidence for Pressure-Induced Metallization in FeO
 295 with Rocksalt-Type Structure. *Phys. Rev. Lett.* **108** (2012).
 296